https://doi.org/10.1016/j.apcatb.2020.118927

Copper Phosphosulfides as a Highly Active and Stable Photocatalyst for Hydrogen Evolution Reaction

Xiandi Zhang,[1,†] Kyung-Ah Min,[2,†] Weiran Zheng,[1] Jeemin Hwang,[2] Byungchan Han,[2,] and Lawrence Yoon Suk Lee[1,3,]**

X. Zhang, Dr. K.-A. Min, Dr. W. Zheng, J. Hwang, Prof. B. Han, Dr. L. Y. S. Lee

[1] Department of Applied Biology and Chemical Technology and the State Key Laboratory of Chemical Biology and Drug Discovery, The Hong Kong Polytechnic University, Hung Hom, Kowloon, Hong Kong SAR

[2] Department of Chemical and Biomolecular Engineering, Yonsei University, Seoul, Republic of Korea

[3] The Hong Kong Polytechnic University Shenzhen Research Institute

† These authors contributed equally to this work.

* E-mails: bchan@yonsei.ac.kr (B. Han); lawrence.ys.lee@polyu.edu.hk (L. Y. S. Lee)

Abstract

Transition-metal phosphosulfides (TMPSs) have recently shown outstanding electrocatalytic performances toward hydrogen evolution reaction (HER), superior to the sulfide and phosphide counterparts. However, there are only limited TMMSs available due to the synthetic challenge. Herein, we demonstrate a novel synthetic approach for copper phosphosulfide (CuPS) and the first application in photocatalytic HER. Based on the thermodynamic considerations of starting

materials, two synthetic routes are designed to obtain two distinct crystal structures (CuS|P and Cu3P|S). Dramatically enhanced photocatalytic HER activities are achieved for both Cu3P|S (2,085 μmol·g-1·h-1) and CuS|P (976 μmol·g-1·h-1) without using co-catalysts. First-principles calculations unveil underlying mechanism of the improved HER activity, in which the Gibbs free energy of hydrogen adsorption approaches close to 0 eV and the number of active sites considerably increases with the formation of CuPS structure. This work provides new insight and design principle on preparing TMPSs for high-performance energy conversion applications.

KEYWORDS: copper phosphosulfide; wet chemical approach; photocatalysis; hydrogen evolution reaction; DFT calculations

Graphical abstract

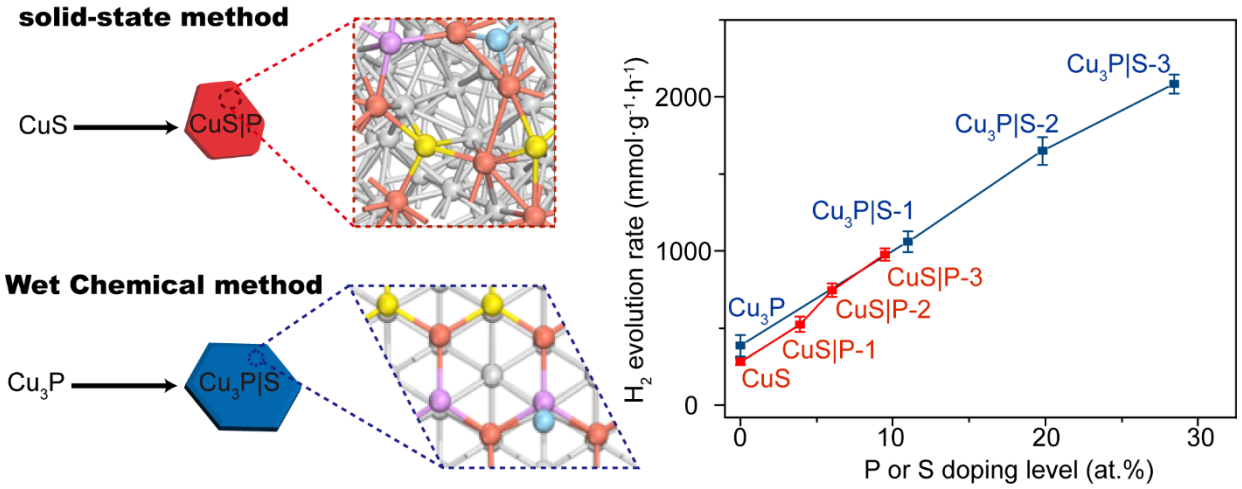

Highlights

- Two copper phosphosulfides (CuS|P and $Cu_3P|S$) are synthesized using conventional solid-state and novel wet chemical approaches.
- The new structure, copper phosphosulfide, exhibits an excellent performance in photocatalytic hydrogen evolution reaction (HER).
- The HER activity is correlated to the formation level of phosphosulfide structure that shifts the Gibbs free energy of hydrogen adsorption close to 0 eV and considerably increases the number of active sites.

1. Introduction

Ever-increasing demand for high quality energy sources and the concerns on environmental degradation issues have driven the global efforts on seeking sustainable and renewable energy materials and devices.[1] Hydrogen is considered as one of the most promising next-generation fuels due to its high energy density, recyclability, and the zero-emission of pollutant.[2,3] Among various techniques developed so far, the photocatalytic water splitting offers the most eco-friendly way of producing hydrogen fuel,[4,5] while its wide application is largely limited by the cost, scarcity, efficiency, and durability of photocatalysts.[6-8] It is, therefore, highly desirable to address the challenge by innovative design of new photocatalysts that are based on earth-abundant elements yet as efficient and stable as noble metal-based ones.

Recently, a variety of transition metal compounds have shown high efficiencies for photocatalytic hydrogen evolution reaction (HER), which include nitrides,[9,10] carbides,[11,12] chalcogenides,[13,14] and phosphides.[15,16] Transition metal phosphosulfides (TMPSs) are the newly emerging family of electrocatalysts, which are gaining great interests owing to their superior catalytic activities and stability compared with the corresponding sulfide or phosphide forms.[17-22] In 2014, molybdenum phosphosulfide (MoP|S) retaining the molybdenum phosphide (MoP) crystal structure was prepared by Jaramillo *et al.*[17] *via* the surface modification of MoP, showing the superb activity and stability for electrocatalytic HER. Similar HER performance enhancement was achieved by using cobalt phosphosulfide (CoS|P) of the CoS crystal structure[18] and the amorphous CoS|P shell on CoP core.[19] Two different crystal structures of iron phosphosulfide were also investigated to show that the surface phosphosulfide (PS) structure play an important role in stabilizing and boosting the electrocatalytic HER performance.[20] The beneficial interaction between S and P partially transfers the electrons from P to S due to different electronegativity,

subsequently tuning each other's electronic properties to produce an active catalyst phase, where the surface oxidation of active sites is mitigated to endow also a good durability.[17,19]

Although the PS structures have shown good performances in the field of (photo)electrochemical hydrogen production,[17-22] recently extending the application to lithium sulfur battery,[23] it is so far limited to only a few transition metals, often with a restricted formation level, due to the difficulties in synthetic process.[18,19] Currently, the preparation method for most TMPSs, if not all, engages the solid-state chemical method, in which a mixture of metal precursors and S and/or P sources is annealed at a high temperature, usually between 400 and 700 °C. Such harsh thermodynamic conditions required for the solid-state method make it a great challenge to tune the structure and property of TMPSs for their extended applications, such as photocatalytic HER. In addition, the reported TMPSs were usually prepared on a conductive supporting material to attain the good electrical conductivity in an electrocatalytic system, further complicating the control of PS structure. Indeed, most TMPSs prepared so far have a core-shell structure, where the PS structure is mostly confined on the surface with a relatively lower percentage than the starting mother structure. Recently, 2D layered metal phosphorus trichalcogenides (MPS_3, where M = Fe and Mn) have been prepared by chemical vapor deposition (CVD) or chemical vapor transport (CVT) method.[24,25] The synthesis of this new class of materials is not trivial and requires high energy for vaporization, as well as a careful optimization of temperature as P atom has to be vaporized along with S atoms and completely react with the metal oxide precursor. The general method for preparing TMPS with the control of PS structure level and distribution is still not available, which may result in limiting their wide application.

Herein, we demonstrate the synthesis of novel copper-based TMPSs with the control of PS formation level under mild conditions and their application in photocatalytic HER as the first

example for TMPS with integrated quantum mechanical calculations and experimental materializations. Starting from Cu_3P and CuS, both of which possess appropriate electronic structures for photocatalysis,[26,27] two distinct structures of copper phosphosulfide ($Cu_3P|S$ and CuS|P) are prepared. To tune the PS formation level, both conventional solid-state reaction and newly developed wet-chemical methods are systematically investigated considering the thermodynamic properties of starting materials. With the new method, the PS structure formation is much facilitated to reach the formation level of *ca*. 29 %, compared with *ca*. 9 % of the conventional method, which is evenly distributed over thin nanoplate structure. We show that the degree of PS formation largely depends on the starting materials and synthetic routes, which substantially affects the photocatalytic HER performance. Using first-principles density functional theory (DFT) calculations, we reveal two underlying mechanisms for photocatalytic activity of copper phosphosuflide: (i) the Gibbs free energy (ΔG_{H*}) of hydrogen adsorption lying close to 0 eV and (ii) increased number of active sites for HER with increasing formation % of PS structure. Both experimental and DFT calculations results indicate the formation of PS structure from both Cu_3P and CuS provides highly active sites for photocatalytic HER.

2. Experimental Section

2.1 Chemicals

Copper (I) chloride (CuCl, 97%), copper (II) acetylacetonate ($Cu(acac)_2$, 95%), oleylamine (OLA, 70%)), trioctylphosphine (TOP, 97%), trioctylphosphine oxide (TOPO, 90%), sodium hypophosphite monohydrate ($NaH_2PO_2 \cdot H_2O$, 99%), *o*-dichlorobenzene (DCB, 99%), and oleic acid (78%) were purchased from Sigma Aldrich. The elemental sulfur (99.98%) was purchased from Arcos. All chemicals were used without further treatment.

2.2 Synthesis of Cu_3P and $Cu_3P|S$

Cu_3P was synthesized following the literature procedure with a slight modification.[28] In a typical procedure, CuCl (1 mmol) and TOPO (2.58 mmol) were dissolved in OLA (5 mL) and heated to 100 °C under N_2 gas for 30 min. At an increased temperature of 150 °C, TOP (1.12 mL) was injected under magnetic stirring and reacted for 5 min. The reaction mixture was purged with PH_3 gas at 230 °C, which was generated by heating NaH_2PO_2 (4.7 mmol) in a separate round bottom flask at 250 °C in the N_2 atmosphere. After 20 min of reaction, the temperature was lowered and kept at 200 °C for 15 min. The reaction solution was then cooled down, and the product was collected by centrifugation, followed by washing with acetone three times. A similar procedure was taken for the synthesis of $Cu_3P|S$ except that a pre-determined amount of elemental sulfur dissolved in DCB (1 mL) was injected into the reaction solution after purging PH_3 gas. The temperature was lowered and kept at 200 °C for 15 min. After cooling down, the product was collected by centrifugation, followed by washing with acetone three times.

2.3 Synthesis of CuS and CuS|P

A modified Ghezelbash's method[29] was adapted for the synthesis of CuS. In a typical procedure, $Cu(acac)_2$ (0.5 mmol) was dissolved in DCB (7 mL) and heated to 110 °C under N_2 atmosphere. To this solution, a mixture of OLA (1.98 mL) and oleic acid (0.075 mL) was injected and stirred for 30 min. The elemental sulfur (2 mmol) dissolved in DCB (3 mL) was transferred to the reaction solution and the temperature was raised to 180 °C for 1 h. The solution was then naturally cooled down to room temperature and the sample was collected by centrifugation, followed by washing with hexane and acetone three times. To prepare CuS|P, as-synthesized CuS (0.4 mmol) was mechanically ground with a pre-determined amount of $NaH_2PO_2 \cdot H_2O$ using a mortar and pestle. The solid mixture was then annealed in a tube furnace at 350 °C for 20 min

under an Ar flow.

2.4 Material Characterization

Powder X-ray diffraction (XRD) patterns were obtained using a Rigaku SmartLab X-ray diffractometer with Cu Kα radiation. The spectra were collected from 2θ of 20° to 70° with a step size of 0.02° at a rate of 10° min^{-1}. Transmission electron microscopic (TEM) images were taken using a JEOL JEM-2100F STEM operated at 200 kV. Samples for TEM analysis were prepared by drop-casting the nanocrystals dispersed in chloroform onto a holey carbon-coated 400 mesh Ni TEM grid. The elemental compositions and distribution were determined by an energy dispersive X-ray spectroscopy (EDX) equipped in TEM. UV-Vis diffuse reflectance spectra were measured using a Cary 4000 UV-Vis Spectrophotometer. X-ray photoelectron spectroscopy (XPS) was conducted using an X-ray Photoelectron Spectrometer (ESCALAB 250Xi, Thermo Fisher) with a monochromic Al Kα X-ray source and a pass energy of 1486.6 eV.

2.4 Electrochemical measurements

Catalyst ink was prepared by dispersing the as-prepared product (3 mg) in a mixture of deionized water (480 μL), ethanol (480 μL), and Nafion (40 μL, 5 wt.%, Sigma-Aldrich) followed by sonication for 30 min. The ink (100 μL) was drop-cast onto a carbon fiber paper (1 cm × 1 cm) which was used as a working electrode. Electrochemical measurements were conducted in a three-electrode system using a CHI 700E electrochemical station where a saturated calomel electrode (SCE) and graphite were used as the reference and counter electrodes, respectively, in phosphate buffer (pH = 7.4).

2.5 Photocatalytic hydrogen generation

As-prepared catalyst (1 mg) was dispersed in an aqueous solution (25 mL) containing the sacrificial agent of 0.35 M Na_2S + 0.25 M Na_2SO_3. After degassing with Ar for 30 min, the

suspended solution was then irradiated with a solar simulator (Newport, 150 W solar simulator, 1 sun) equipped with an AM 1.5 air mass filter. The reaction product in the headspace was periodically sampled with a gastight syringe and analyzed by an Agilent 7890 B gas chromatograph equipped with a thermal conductivity detector (TCD) using nitrogen as the carrier gas.

2.6 First-principles calculations

We extensively utilized the first-principles density functional theory (DFT) calculations to understand the underlying mechanisms for the enhanced photocatalytic HER activity of the copper phosphosulfides. The calculations were performed within a generalized gradient approximations (GGA) for exchange-correlation (*xc*) functionals,[30,31] implemented in the Vienna *ab* initio simulation package (VASP).[32,33] The kinetic energy cut-off was set to 400 eV, and the electron-ion interactions were described by projector augmented wave (PAW) potentials.[34] The Grimme's DFT-D3 method[35] based on a semi-empirical GGA-type theory was adopted for van der Waals (vdW) corrections. In the calculations, we considered (1 × 1) and (2 × 2) times surface unit cells of $Cu_3P(1\bar{1}0)$ and CuS(001) which have the lowest surface energies in their bulk crystal structures, respectively. Then, a H atom was adsorbed on both $Cu_3P(1\bar{1}0)$ and CuS(001) surfaces with H coverages of 12.5 %. Our DFT calculations showed that H atoms spontaneously adsorb on the surfaces with Gibbs free energies in range from -0.36 to -0.11 eV. For the Brillouin-zone integration, (6 × 6 × 1) grids in the reciprocal space were used for both $Cu_3P(1\bar{1}0)$ and CuS(001) with the Gamma centered scheme. We setup seven layers slab models for $Cu_3P(1\bar{1}0)$ and CuS(001) surfaces, and all atoms except for the bottommost four layers were fully optimized until the Hellmann-Feynman forces and energies were converged within 0.02 eV/Å and 1×10^{-5} eV, respectively.

To identify the HER photocatalytic activities depending on the surface formation levels in $Cu_3P(1\bar{1}0)$ and CuS(001) surfaces, we calculated Gibbs free energy (ΔG_{H^*}) of H adsorption using following equation (1):

$$\Delta G_{H*} = E_{ads} + \Delta E_{ZPE} - T\Delta S \qquad (1)$$

, where E_{ads}, ΔE_{ZPE}, ΔS, and T are the adsorption energy of hydrogen atom, zero-point energy correction and entropy change by the adsorption, and temperature, respectively. Here, $\Delta E_{ZPE} - T\Delta S$ was approximated to 0.29 eV.[36] The E_{ads} was defined as

$$\mathrm{E_{ads}} = E_{H+surf} - E_{surf} - \frac{1}{2}(E_{H_2}) \qquad (2)$$

where E_{H+surf}, E_{surf}, and E_{H2} are the energies of H adsorption on Cu_3P (or CuS), isolated Cu_3P (or CuS), and H_2 molecule, respectively. Using the scheme proposed by Nørskov et al.,[37] ΔE_{ZPE} and ΔS were obtained by following equation (3) and (4):

$$\Delta E_{ZPE} = E_{ZPE}(H^*) - \frac{1}{2}E_{ZPE}(H_2) \qquad (3)$$

$$\Delta S = S(H^*) - \frac{1}{2}S(H_2) \approx -\frac{1}{2}S(H_2) \qquad (4)$$

Here, ΔS is approximated to $-\frac{1}{2}S(H_2)$ due to the negligible vibrational entropy of adsorbed H; $T\Delta S$ is obtained to be *ca*. -0.20 eV at 298 K and 1 bar, with the entropy of gaseous H_2 in standard states. Using the first-principles DFT calculations, ΔE_{ZPE} were calculated to be *ca*. 0.09 and 0.05 eV for the adsorbed H on CuS and Cu_3P, respectively. Therefore, $\Delta E_{ZPE} - T\Delta S$ were approximated to 0.29 and 0.25 eV for the H adsorption on CuS and Cu_3P, respectively.

3. Results and Discussion

Scheme 1 illustrates two synthetic approaches engaged to prepare copper phosphosulfides (CuPSs), using either CuS or Cu_3P as a host crystal structure for P or S insertion, respectively. As we discuss later, the success of phosphosulfide (PS) formation largely depends on the synthetic method. In a typical solid-state reaction method (Route A in **Scheme 1**), the pre-formed CuS is mechanically ground with the various amount of NaH_2PO_2 (12.5, 75, 165, and 237.5 mol% of CuS) and annealed at 350 °C to yield products (denoted as CuS|P-1, CuS|P-2, CuS|P-3, and CuS|P-4, respectively). The energy dispersive X-ray spectroscopic (EDX) analyses confirm the existence of P atoms in the CuS|P samples (**Figure S1a**). The atomic % of P in CuS|P samples almost linearly increases with the amount of NaH_2PO_2 used (3.9% in CuS|P-1, 6.0% in CuS|P -2, 9.5% in CuS|P-3, and 9.7 % in CuS|P -4). In contrast, the S atomic % shows a monotonic decrease with the amount of P precursor used, from 47.3 % in CuS to 23.2 % in CuS|P-4, indicating the replacement of S by P atoms.[20]

In a reversed reaction where Cu_3P is annealed with S source, however, such P-to-S substitution is not observed, because Cu_3P has the higher thermal stability than CuS (ΔH_f for CuS and Cu_3P are -79.5 and -116.1 $kJ \cdot mol^{-1}$ at 298 K, respectively).[38,39] To circumvent this thermodynamic barrier, a wet chemical method is designed to introduce the S precursor during the growth of Cu_3P (Route B, **Scheme 1**). Various amount of elemental S (3.3, 16.7, 33.3, 50.0 mol% of Cu_3P) has been added to the Cu_3P seed solution[26] to successfully yield the CuPS of Cu_3P-type crystal structure (denoted as Cu_3P|S-1, Cu_3P|S-2, Cu_3P|S-3, and Cu_3P|S-4, respectively). The incorporation of S atoms into Cu_3P is supported by EDX analyses (**Figure S1b**) where the S atomic % increases with the amount of S precursor (11.0% in Cu_3P|S-1, 19.8% in Cu_3P|S-2, 28.4% in Cu_3P|S-3, and 36.8% in Cu_3P|S-4), while P atomic % decreases from 28.3 % in Cu_3P to 14.0 % in Cu_3P|S-4. It is worth to note that much higher PS formation levels are achieved with the use of

less precursor compared to the solid-state reaction method.

The morphology of CuS|P and Cu_3P|S samples are examined by transmission electron microscopy (TEM) and compared in **Figures 1** and **S2**. The CuS prepared without P coordination exhibits a hexagonal or truncated triangle plate with edges ranging from 36 to 55 nm (**Figure 1a**). The incorporation of small amount of P has no obvious effect on the CuS morphology (CuS|P-1 and CuS|P-2) although the edges are slightly blunted. With higher P atomic %, the shape of CuS|P-3 is changed to the rounded plate (**Figure 1d**), which is probably caused by larger atomic size of P (P: 108 pm, S: 106 pm).[20] High-resolution TEM (HR-TEM) images (insets in **Figure 1**) clearly reveal the lattice fringes with unchanged *d*-spacing of 1.91 Å that corresponds to the (107) planes of CuS,[29] indicating that the CuS structure is still retained. The TEM image of CuS|P-4 shows merged nanoplates with ill-defined edges and increased *d*-spacing (1.95 Å), suggesting the structural change due to high atomic % of P (**Figure 1e**). Despite the variation in shape, all CuS|P samples display evenly distributed Cu, P, and S atoms from the EDX-mapping (**Figure S3a**).

Figure 1f shows the as-synthesized hexagonal Cu_3P nanoplates with the edge lengths of *ca*. 75 nm. Although the edges lose their sharpness as more S is introduced, the hexagonal shape is mostly well maintained up to the S atomic % of 28.4 % (**Figures 1g-i**), due to mild reaction conditions (230 °C) and the presence of capping ligands (TOP and TOPO). The lattice fringes with *d*-spacing of 2.02 Å are evident from the HR-TEM images of Cu_3P|S-1 to Cu_3P|S-3 (insets in **Figures 1g-i**), which matches the interplanar distance of (300) planes in Cu_3P.[28] However, further increased S atomic % in Cu_3P|S-4 leads to the morphology destruction to aggregated smaller nanoparticles that exhibit different *d*-spacing (1.95 Å, **Figure 1j**). The co-existence of Cu, P, and S atoms evenly distributed in all Cu_3P|S sample are confirmed by EDX-mapping (**Figure S3b**).

To verify the crystal phase transition suggested by TEM images, X-ray diffraction (XRD)

patterns of samples are measured as presented in **Figure 2**. The pristine CuS exhibits the diffraction peaks at 29.3°, 31.8°, 32.9°, 47.8°, 48.0°, and 59.3°, corresponding to (102), (103), (006), (107), (110), and (116) planes of CuS (PDF# 06-0464, **Figure 2a**). After the PH_3 treatment, two new peaks at 46.1° and 54.6° appeared in CuS|P-1 to CuS|P-3, which belong to (220) and (311) facets of $Cu_{1.8}S$ (PDF#24-0061), and intensify with the P atomic % increasing. The formation of $Cu_{1.8}S$ is most likely due to the partial reduction of CuS by reductive PH_3.[40] Upon the reaction with PH_3, the Cu-S bond in CuS is first broken and S vacancies are created ($Cu_{2-x}S$) with which the P atoms can coordinate to form PS structure. More importantly, no Cu_3P traits are observed after the PH_3 treatment, an indication of atomic replacement of S by P. In addition, slight but obvious peak shifts to lower 2θ values are observed in CuS|P-1 to CuS|P-3, which also varies as a function of P atomic % (right panel of **Figure 2a**). For instance, the merged peak of (107) and (110) shifts from 48.0° to 47.8° (CuS|P-3), probably due to replacement of S atoms with larger P atoms.[20,41,42] This is supported by the expansion of unit cell volume of original CuS from 228.15 $Å^3$ to 231.11 $Å^3$ in CuS|P-1, 239.79 $Å^3$ in CuS|P-2, and 243.88 $Å^3$ in CuS|P-3 (**Figure 2b** and **Table S1**). Meanwhile, this peak shift is accompanied by the gradual peak broadening and intensity decrease, which can be reasoned with the degradation of crystallinity due to the lattice disorder and strain induced by P atoms.[43] The excessive PH_3 treatment in CuS|P-4 results in the crystal structure conversion, as indicated by its XRD pattern showing the peaks at 37.3°, 45.7°, 48.1°, and 53.5°, corresponding to (102), (110), (103), and (112) facets of Cu_2S (PDF# 46-1195). This is consistent with the HR-TEM observation where the observed *d*-spacing of 1.95 Å can be attributed to (110) plane of Cu_2S.

Figure 2c compares the XRD patterns of Cu_3P and $Cu_3P|S$ samples. The pristine Cu_3P shows the diffraction peaks at 36.1°, 39.2°, 41.8°, 45.1°, 46.1°, and 47.3° assigned to (112), (202), (211), (300), (113), and (212) planes of Cu_3P (PDF# 02-1263).[28] The $Cu_3P|S$ samples, except for $Cu_3P|S$-

4, exhibit similar diffraction patterns as Cu_3P without any additional peak, assuring that no other sulfide phase has formed. However, as S atomic % increases, the diffraction peaks progressively shift to higher 2θ values (right panel of **Figure 2c**). In particular, two most intense peaks from (300) and (113) planes shift from 45.1° and 46.1° (Cu_3P) to 45.3° and 46.2° (Cu_3P|S-3), respectively. From the lattice refinement of the XRD data (**Figure 2d** and **Table S2**), it is evident that the volume of Cu_3P unit cell (348.80 $Å^3$) gradually decreases to 344.11 $Å^3$ (Cu_3P|S-1), 338.58 $Å^3$ (Cu_3P|S-2), and 323.81 $Å^3$ (Cu_3P|S-3) with S atomic %. The partial replacement of the larger atomic size of P by the smaller atomic size of S is believed to cause this lattice change.[41-42] Based on the suggestions from EDX and XRD, the Cu_3P|S can allow a 28.4% of P replacement by S without losing the initial Cu_3P crystal structure, but with lattice disorder in unit cell, resulting in the degradation of crystallinity and thus showing obvious peak broadening.[43] With the highest S substitution of 36.75% (Cu_3P|S-4), however, the XRD pattern suggests that the Cu_3P structure has been lost. The diffraction peaks at 37.3°, 45.7°, and 48.1° are assigned to (102), (110), and (103) planes of Cu_2S (PDF# 46-1195). In general, the wet chemical approach allows not only the S coordinate on Cu_3P to yield Cu_3P|S but also the higher coordination levels in comparison with solid-state reaction method.

We engaged the X-ray photoelectron spectroscopy (XPS) to investigate the states of surface species on CuS|P and Cu_3P|S and validate the CuPS formation. The surface P/S atomic % determined by the XPS is in good agreements with the bulk P/S ratio obtained using the EDX **(Table S3**), confirming that the PS structure is uniformly distributed within the nanoplates rather than forming a shell-like structure.[18] Furthermore, the XPS survey spectra shown in **Figure S4** confirm the existence of Cu, P, and S in both CuS|P and Cu_3P|S samples. The Cu 2p spectrum of CuS|P-3 (**Figure 3a**, top) displays two sets of Cu $2p_{3/2}$ and $2p_{1/2}$ peaks. The fitted peaks at 933.0

and 953.1 eV correspond to the Cu^{2+} species of CuS (**Figure 3a**, bottom), while those at 932.0 and 951.9 eV are assigned to Cu^{+}, suggesting the formation of Cu-P bond.[44] This is supported by the P 2p spectrum where the P^{3-} species is confirmed by the peaks at 129.8 and 130.7 eV (**Figure 3c**).[19,45] The P-O species due to surface oxidation is also observed at 133.6 eV. The CuS|P-3 also shows a much broader S 2p signature than CuS, which are deconvoluted to two groups of peaks (**Figure 3b**, top). The first pair (161.7 and 162.8 eV) is assigned to S^{2-} species corresponding to CuS, while the second group at 163.5 and 164.6 eV is ascribed to S_2^{2-} arising from the S-S bond in $Cu_{2-x}S$.[46,47] This agrees well with TEM and XRD results that indicate the reduction of Cu^{2+} with P coordination.

In the case of Cu_3P|S-3, a similar Cu 2p spectrum as in Cu_3P is obtained with two main Cu $2p_{3/2}$ and $2p_{1/2}$ peaks at 932.1 and 951.9 eV, respectively, well matching the Cu^{+} species in Cu_3P (**Figure 3d**).[48] The peak fitting, however, reveals another set of small Cu $2p_{3/2}$ and $2p_{1/2}$ peaks at 933.4 and 953.4 eV, which is ascribed to Cu^{2+} state due to the Cu-S formation.[44] The S 2p spectrum of Cu_3P|S-3 clearly shows S $2p_{3/2}$ and $2p_{1/2}$ peaks at 161.7 and 162.8 eV, respectively, corresponding to S^{2-}, which is absent in pristine Cu_3P (**Figure 3e**).[44] Two types of P species are evident from the P 2p spectra of Cu_3P and Cu_3P|S-3 (**Figure 3f**). The P $2p_{3/2}$ and $2p_{1/2}$ peaks at 129.7 and 130.6 eV are assigned to P^{3-} arising from Cu-P bond, while another peak at 133.8 eV is attributed to P-O bond due to the surface oxidation.[19] Interestingly, the relative peak area of P-O species is reduced after introducing S, suggesting the better stability of Cu_3P|S than pristine Cu_3P in the air.[49]

The CuPSs prepared from CuS and Cu_3P are demonstrated to possess different PS formation levels, crystal structures, and surface species compositions, which would impose unique optical and electronic properties. The effect of such differences is investigaved by carrying out the

photocatalytic HER, and the results are summarized in **Figure 4**. Both CuS|P and Cu_3P|S samples exhibit dramatically enhanced photocatalytic HER activities compared to their structural analogs, which escalate proportional to the PS formation levels (**Figure S5**). The HER rate of pristine CuS is merely 280 $\mu mol \cdot g^{-1} \cdot h^{-1}$, which increases to 528 $\mu mol \cdot g^{-1} \cdot h^{-1}$ upon 3.9 % PS formation (CuS|P-1) and reaches a maximum of 976 $\mu mol \cdot g^{-1} \cdot h^{-1}$ with CuS|P-3. This is nearly 350 % enhancement of HER rate with 9.5 % PS formation on CuS. The photocatalytic HER activities of Cu_3P|S samples show even higher promotion effects. The Cu_3P|S-3 has reached a maximum HER rate of 2,085 $\mu mol \cdot g^{-1} \cdot h^{-1}$, more than a five-fold increase compared to pristine Cu_3P (385 $\mu mol \cdot g^{-1} \cdot h^{-1}$). These HER rates mark the highest among the recently developed Cu-based photocatalysts, including sulfides, phosphides, and oxides (**Table S4**). This remarkable enhancement of catalytic performance is achieved without changing the crystal structure or using any co-catalyst. It can be correlated to the Cu_3P structure that hosts a high PS formation level (28.4% S in Cu_3P|S-3), hence allowing the formation of CuPS structure to a greater extent. Meanwhile, in a control experiment where a physical mixture of CuS and Cu_3P with the identical P:S ratio is used (**Figure S6**), such a boost of HER activity is not observed. Also, in the absence of CuPS catalyst, only negligible amount of H_2 (0.073 $\mu mol \cdot g^{-1}\ h^{-1}$) is detected due to the activity of sacrificial agent. In the stability aspect, both CuS|P and Cu_3P|S samples show no apparent activity loss during the continuous 24 h reactions, as illustrated in **Figures 4c** and **d**. The characterizations of both samples after 24 h photocatalytic reaction confirm the unchanged crystal structure, morphology, and composition (**Figure S7** and **S8**), demonstrating their exceptional stability toward photocorrosion.

One of the known mechanisms of promoting the photocatalytic performance is to enhance the optical properties of catalyst, usually by band gap engineering to better utilize the sunlight and/or suit the required potential for target reaction. In order to further understand the HER promoting

effect, we first studied their optical band structures by UV-Vis diffraction reflectance spectra (DRS). **Figure S9a** compares the absorption spectra of CuS and CuS|P samples, where the characteristic surface plasmon resonance (SPR) absorption (550 - 700 nm) of CuS disappears with forming PS structure. The corresponding Tauc plot (**Figure S9b**) indicates that the band gap of CuS|P is slightly decreased to *ca*. 1.93 eV from 2.11 eV of CuS. This can be explained by the formation of $Cu_{1.8}S$ that has a narrower band gap of 1.8 eV and weaker SPR effect than CuS.[46,50,51] On the other hand, the PS formation in Cu_3P appears to have no obvious influence on the light absorption as indicated by the same band gap of $Cu_3P|S$ as Cu_3P (1.52 eV),[52] **Figures S9c** and **d**). The formation of CuPS in both cases seems to have minimal effects on the band gap energy, which rules out the optical property change from the major reason for the dramatic promotion of HER performance. It is reasonable to believe that the surface composition and thus the local environments of active site have a more significant impact on the HER performance, as it involves the surface reaction.

In general, catalytic activity critically depends on the number of active sites for desired reaction. To identify active sites for HER, we calculated the free energy of H adsorption, which is the first elementary step of the HER, using DFT calculations. To simulate our experimental process for the catalyst design, we set up two model catalysts of CuS (or Cu_3P) by different doping levels of P or S: one atomic doping per unit cell (CuS|P and $Cu_3P|S$), and two (CuS|2P and $Cu_3P|2S$). Our DFT calculations indicate that the CuPS surfaces possess vastly different surface properties from the pristine one of CuS or Cu_3P. Most important one is that electronic charges dissimilarly distributes in the surfaces of CuPS/CuS (CuS|P) and CuPS/Cu_3P ($Cu_3P|S$), which substantially affects the adsorption of H. Our calculations show that H thermodynamically prefers to adsorb on S of un-doped CuS (**Figure 5a)**. The adsorption site is, however, switched to atop of the doped P

in CuS|P and CuS|2P; H adsorption is stronger in the P than S with remarkable charge transfer from P to H atoms (**Figure S10**). It means that the PS formation in CuS is a better way to improve HER activity. Additionally, the Gibbs free energy for H adsorption (ΔG_{H^*}) in the P site is located at closer to 0 eV with increasing the PS formation level, as shown in **Figure 5c** and **Table S5**; especially, ΔG_{H^*} is equal to -0.19 eV in CuS|2P. Furthermore, with the PS formation level increased, Cu is also activated as clearly shown by the reduced ΔG_{H^*} (closer to 0) from 1.34 (CuS and CuS|P) to 0.61 eV (CuS|2P, **Table S5)**. It is noteworthy that the enhanced HER activity in part comes by the increased numbers of active sites.

For un- and S-doped Cu_3P, adsorption behaviors of H on Cu_3P are slightly different from those of the P-doped CuS surface (**Figure 5b** and **d)**. Our calculations indicate that H atoms preferentially adsorb on hollow sites (Cu_h) in Cu_3P, regardless of the formation level of PS (**Figure 5b**). Here, we found that there is electronic charge transfer from Cu to H both in pure and S-doped Cu_3P as illustrated in **Figure S11**. Interestingly, ΔG_{H^*} in Cu_h sites lies closer to 0 eV as surface PS formation level increases (**Figure 5d** and **Table S6**); The ΔG_{H^*} slightly changes from -0.11 (Cu_3P and Cu_3P|S) to -0.07 eV (Cu_3P|2S), indicating the improved HER activities at Cu_h sites. Moreover, we identified that ΔG_{H^*} on P site also shifts closer to 0 eV with PS formed in Cu_3P surface. The ΔG_{H^*} on P site decreases from 0.27 (Cu_3P) to 0.14 eV (Cu_3P|2S), due to the electron charge transfer from the surface P to the doped S by the electronegativity difference; electronic charge of P decreased from 5.55e (Cu_3P) to 5.48 eV (Cu_3P|2S, **Figure S11)**. The electronic structures push the ΔG_{H^*} to be closer to 0 by enhancing H adsorption energy at the P atom. In summary, our calculations poise that both P and Cu_h sites interplay as active sites to improve HER catalysis. It means that the doped S not only increases numbers of active sites in the Cu_3P surfaces but also creates a favorable free energy landscape for HER photocatalysis.

This conclusion is also supported with changed electrocatalytic overpotential. **Figure S12** compares the linear sweep voltammogram (LSV) curves measured using as-prepared samples as a working electrode under neutral conditions. The overpotential at a current density of 10 $mA \cdot cm^{-2}$ of CuS|P is 297 mV (vs. reversible hydrogen electrode, RHE), which gradually decreases to 286 mV (CuS|P-1), 271 mV (CuS|P-1), and 246 mV (CuS|P-3). Similarly, the overpotential at 10 $mA \cdot cm^{-2}$ diminishes from 300 mV (Cu_3P) to 238 mV (Cu_3P|S-3) with the formation of PS structure in Cu_3P. Such reduced overpotentials observed with CuS|P-3 and Cu_3P|S-3 suggest their smaller energy barrier on driving the HER catalysis, thus HER can be easier to drive with the formation of PS structure, meaning the enhanced catalytic activity compared to pristine CuS or Cu_3P.

Based on the experimental and DFT calculations results, we proposed the photocatalytic HER mechanism on CuPSs in **Figure S13**. Upon the irradiation, the electrons in the valence band of CuPSs are excited to the conduction band that has more negative potential required for the H^+ reduction to H_2. This is the same mechanism as on Cu_3P or CuS, yet the formation of PS structure makes the ΔG_{H^*} thermodynamically favorable for HER and offers more active sites.

4. Conclusion

In conclusion, two copper phosphosulfides of distinct crystal structures (CuS and Cu_3P) are prepared with a tunable range of S and P atomic ratio by engaging two synthetic routes, the solid-state and novel wet chemical methods. The wet chemical approach provides a mild way of introducing high formation levels of PS in Cu_3P retaining the crystal structure. Both CuS|P and Cu_3P|S exhibit dramatically enhanced photocatalytic activities toward HER, which are closely related to PS formation level. In particular, the Cu_3P|S-3 of 28.4 % PS formation displays a maximum HER rate of 2,085 $\mu mol \cdot g^{-1} \cdot h^{-1}$ that account for more than a five-fold activity boost compared to pristine Cu_3P. Our DFT calculations shows that the phosphosulfide structures drive

the Gibbs free energies (ΔG_{H^*}) for the intermediate states to be close to 0 eV and increase the number of active sites for H adsorption, leading to the highly improved catalytic activity toward HER. This work provides new insights on the synthetic approaches for high-performance TMPSs and the fundamental understanding for enhanced HER activities.

Acknowledgments

This research was supported by The Hong Kong Polytechnic University (Grant No. 1-BE0Y), Shenzhen Science, Technology and Innovation Commission (SZTIC, JCYJ20170818105046904), and the Global Frontier Program through the Global Frontier Hybrid Interface Materials (GFHIM) of National Research Foundation of Korea (NRF) funded by the Ministry of Science and ICT (Project No. 2013M3A6B1078882).

Supporting Information

Supporting Information including EDX-mapping, lattice parameters, XPS, post-HER XRD and TEM, UV-Vis DRS spectra and Tauc plots, and the charge analyses by DFT calculations is available from online version.

Conflict of Interest

The authors declare no conflict of interest.

References

[1] N. Lewis,D. Nocera, Powering the planet: Chemical challenges in solar energy utilization, Proc. Natl. Acad. Sci. 103 (2006) 15729-15735.

[2] S. Yu, X. Fan, X. Wang, J. Li, Q. Zhang, A. Xia, S. Wei, L. Wu, Y. Zhou, G. Patzke, Efficient photocatalytic hydrogen evolution with ligand engineered all-inorganic InP and InP/ZnS colloidal quantum dots, Nat. Commun. 9 (2018) 4009.

[3] Y. Gao, X. Li, H. Wu, S. Meng, X. Fan, M. Huang, Q. Guo, C. Tung, L. Wu, Exceptional Catalytic Nature of Quantum Dots for Photocatalytic Hydrogen Evolution without External Cocatalysts, Adv. Funct. Mater. 28 (2018) 1801769.

[4] M. Ni, M. Leung, D. Leung, K. Sumathy, A review and recent developments in photocatalytic water-splitting using TiO_2 for hydrogen production, Renewable Sustainable Energy Rev. 11 (2007) 401-425.

[5] M. Bhatt,J. Lee, Nanomaterials for photocatalytic hydrogen production: from theoretical perspectives, RSC Adv. 7 (2017) 34875-34885.

[6] X. Chen, S. Shen, L. Guo, S. Mao, Semiconductor-based photocatalytic hydrogen generation, Chem. Rev. 110 (2010) 6503-6570.

[7] L. Yuan, C. Han, M. Yang, Y. Xu, Photocatalytic water splitting for solar hydrogen generation: fundamentals and recent advancements, Int. Rev. Phys. Chem. 35 (2016) 1-36.

[8] C. Chen, W. Ma, J. Zhao, Semiconductor-mediated photodegradation of pollutants under visible- light irradiation, Chem. Soc. Rev. 39 (2010) 4206-4219.

[9] B. Cao, G. Veith, J. Neuefeind, R. Adzic, P. Khalifah, Mixed close-packed cobalt molybdenum nitrides as non-noble metal electrocatalysts for the hydrogen evolution reaction, J. Am. Chem. Soc. 135 (2013) 19186-19192.

[10] W. Chen, K. Sasaki, C. Ma, A. Frenkel, N. Marinkovic, J. Muckerman, Y. Zhu, R. Adzic, Hydrogen-evolution catalysts based on non-noble metal nickel–molybdenum nitride nanosheets, Angew. Chem. Int. Ed. 51 (2012) 6131-6135.

[11] Q. Gong, Y. Wang, Q. Hu, J. Zhou, R. Feng, P. Duchesne, P. Zhang, F. Chen, N. Han, Y. Li, Ultrasmall and phase-pure W_2C nanoparticles for efficient electrocatalytic and photoelectrochemical hydrogen evolution, Nat. Commun. 7 (2016) 13216.

[12] H. Vrubel,X. Hu, Molybdenum boride and carbide catalyze hydrogen evolution in both acidic and basic solutions, Angew. Chem. 124 (2012) 12875-12878.

[13] T. Jaramillo, K. Jørgensen, J. Bonde, J. Nielsen, S. Horch, I. Chorkendorff, Identification of active edge sites for electrochemical H_2 evolution from MoS_2 nanocatalysts, Science 317 (2007) 100-102.

[14] K. Kwon, S. Choi, J. Lee, K. Hong, W. Sohn, D. M. Andoshe, K. S. Choi, Y. Kim, S. Han, S. Y. Kim, Drastically enhanced hydrogen evolution activity by 2D to 3D structural transition in anion-engineered molybdenum disulfide thin films for efficient Si-based water splitting photocathodes, J. Mater. Chem. A 5 (2017) 15534-15542.

[15] E. Popczun, J. McKone, C. Read, A. Biacchi, A. Wiltrout, N. Lewis, R. Schaak, Nanostructured nickel phosphide as an electrocatalyst for the hydrogen evolution reaction, J. Am. Chem. Soc. 135 (2013) 9267-9270.

[16] G. Zhang, G. Wang, Y. Liu, H. Liu, J. Qu, J. Li, Highly active and stable catalysts of phytic acid-derivative transition metal phosphides for full water splitting, J. Am. Chem. Soc. 138 (2016) 14686-14693.

[17] J. Kibsgaard,T. Jaramillo, Molybdenum phosphosulfide: an active, acid-stable, earth-abundant catalyst for the hydrogen evolution reaction, Angew. Chem. Int. Ed. 53 (2014)

14433-14437.

[18] W. Liu, E. Hu, H. Jiang, Y. Xiang, Z. Weng, M. Li, Q. Fan, X. Yu, E. Altman, H. Wang, A highly active and stable hydrogen evolution catalyst based on pyrite-structured cobalt phosphosulfide, Nat. Commun. 7 (2016) 10771.

[19] D. Li, J. Kang, H. Lee, D. Choi, S. Koo, B. Han, S. Kim, High Activity Hydrogen Evolution Catalysis by Uniquely Designed Amorphous/Metal Interface of Core-shell Phosphosulfide/N-Doped CNTs, Adv. Energy Mater. 8 (2018) 1702806.

[20] Z. Wu, X. Li, W. Liu, Y. Zhong, Q. Gan, X. Li, H. Wang, Materials Chemistry of Iron Phosphosulfide Nanoparticles: Synthesis, Solid State Chemistry, Surface Structure, and Electrocatalysis for the Hydrogen Evolution Reaction, ACS Catal. 7 (2017) 4026-4032.

[21] Q. Gan, Z. Wu, X. Li, W. Liu, H. Wang, Structure and Electrocatalytic Reactivity of Cobalt Phosphosulfide Nanomaterials, Top. Catal. 61 (2018) 958-964.

[22] V. Veeramani, H. C. Yu, S. F. Hu, R. S. Liu, Highly Efficient Photoelectrochemical Hydrogen Generation Reaction Using Tungsten Phosphosulfide Nanosheets, ACS Appl. Mater. Interfaces 10 (2018) 17280-17286.

[23] G. Zhou, J. Sun, Y. Jin, W. Chen, C. Zu, R. Zhang, Y. Qiu, J. Zhao, D. Zhuo, Y. Liu, X. Tao, W. Liu, K. Yan, H. R. Lee, Y. Cui, Sulfiphilic Nickel Phosphosulfide Enabled Li_2S Impregnation in 3D Graphene Cages for Li-S Batteries, Adv. Mater. 29 (2017) 1603366.

[24] Z. Cheng, T.A. Shifa, F. Wang, Y. Gao, P. He, K. Zhang, C. Jiang, Q. Liu, J. He, High-Yield Production of Monolayer $FePS_3$ Quantum Sheets via Chemical Exfoliation for Efficient Photocatalytic Hydrogen Evolution, Adv. Mater., 30 (2018) 1707433.

[25] T.A. Shifa, F. Wang, Z. Cheng, P. He, Y. Liu, C. Jiang, Z. Wang, J. He, High Crystal Quality 2D Manganese Phosphorus Trichalcogenide Nanosheets and their Photocatalytic Activity,

Advanced Functional Materials, 28 (2018) 1800548.

[26] Q. Li, F. Wang, L. Sun, Z. Jiang, T. Ye, M. Chen, Q. Bai, C. Wang, X. Han, Design and Synthesis of Cu@CuS Yolk-Shell Structures with Enhanced Photocatalytic Activity, Nano-Micro Lett. 9 (2017) 35.

[27] W. Wang, X. Zhao, Y. Cao, Z. Yan, R. Zhu, Y. Tao, X. Chen, D. Zhang, G. Li, D. Phillips, Copper Phosphide Enhanced Lower Charge Trapping Occurrence in Graphitic-C_3N_4 for Efficient Noble-Metal-Free Photocatalytic H_2 Evolution, ACS Appl. Mater. Interfaces (2019) 16527-16537.

[28] G. Manna, R. Bose, N. Pradhan, Semiconducting and plasmonic copper phosphide platelets, Angew. Chem. 125 (2013) 6894-6898.

[29] A. Ghezelbash,B. A. Korgel, Nickel sulfide and copper sulfide nanocrystal synthesis and polymorphism, Langmuir 21 (2005) 9451-9456.

[30] W. Kohn,L. J. Sham, Self-consistent equations including exchange and correlation effects, Phys. Rev. 140 (1965) A1133.

[31] J. P. Perdew, K. Burke, M. Ernzerhof, Generalized gradient approximation made simple, Phys. Rev. Lett. 77 (1996) 3865-3868.

[32] G. Kresse,J. Furthmüller, Efficient iterative schemes for ab initio total-energy calculations using a plane-wave basis set, Phys. Rev. B 54 (1996) 11169.

[33] G. Kresse,J. Furthmüller, Efficiency of ab-initio total energy calculations for metals and semiconductors using a plane-wave basis set, Comput. Mater. Sci. 6 (1996) 15-50.

[34] P. E. Blöchl, Projector augmented-wave method, Phys. Rev. B 50 (1994) 17953.

[35] S. Grimme, J. Antony, S. Ehrlich, H. Krieg, A consistent and accurate ab initio parametrization of density functional dispersion correction (DFT-D) for the 94 elements H-

Pu, J. Chem. Phys. 132 (2010) 154104.

[36] M. Cabán-Acevedo, M. Stone, J. Schmidt, J. Thomas, Q. Ding, H.-C. Chang, M.-L. Tsai, J.-H. He, S. Jin, Efficient hydrogen evolution catalysis using ternary pyrite-type cobalt phosphosulphide, Nat. Mater. 14 (2015) 1245.

[37] J. K. Nørskov, T. Bligaard, A. Logadottir, J. R. Kitchin, J. G. Chen, S. Pandelov, U. Stimming, Trends in the exchange current for hydrogen evolution. J. Electrochem. Soc. 3 (2005) J23-J26.

[38] S. Boone, O. Kleppa, Determination of the standard enthalpy of formation of Cu_3P by direct-combination drop calorimetry, Thermochim. Acta 202 (1992) 113-119.

[39] D. R. Lide, CRC handbook of chemistry and physics: a ready-reference book of chemical and physical data. CRC Press, Boca Raton, 1995.

[40] X. Feng, P. Wang, J. Hou, J. Qian, Y. Ao, C. Wang, Significantly enhanced visible light photocatalytic efficiency of phosphorus doped TiO_2 with surface oxygen vacancies for ciprofloxacin degradation: Synergistic effect and intermediates analysis, J. Hazard. Mater. 351 (2018) 196-205.

[41] R. Bose, V. Jothi, B. Koh, C. Jung, S. C. Yi, Molybdenum Sulphoselenophosphide Spheroids as an Effective Catalyst for Hydrogen Evolution Reaction, Small 14 (2018) 1703862.

[42] T. N. Khawula, K. Raju, P. J. Franklyn, I. Sigalas, K. I. Ozoemena, Symmetric pseudocapacitors based on molybdenum disulfide (MoS_2)-modified carbon nanospheres: correlating physicochemistry and synergistic interaction on energy storage, J. Mater. Chem. A 4 (2016) 6411-6425.

[43] P. Singh, A. Kaushal, D. Kaur, Mn-doped ZnO nanocrystalline thin films prepared by ultrasonic spray pyrolysis, J. Alloys Compd. 471 (2009) 11-15.

[44] Tarachand, S. Hussain, N. Lalla, Y. Kuo, A. Lakhani, V. Sathe, U. Deshpande, G. Okram, Thermoelectric properties of Ag-doped CuS nanocomposites synthesized by a facile polyol method, Phys. Chem. Chem. Phys. 20 (2018) 5926-5935.

[45] M. Pi, T. Yang, S. Wang, S. Chen, One-pot synthesis of in situ carbon-decorated Cu_3P particles with enhanced electrocatalytic hydrogen evolution performance, J. Mater. Res. 33 (2018) 546-555.

[46] Y. Xie, A. Riedinger, M. Prato, A. Casu, A. Genovese, P. Guardia, S. Sottini, C. Sangregorio, K. Miszta, S. Ghosh, T. Pellegrino, L. Manna, Copper sulfide nanocrystals with tunable composition by reduction of covellite nanocrystals with Cu^+ ions, J. Am. Chem. Soc. 135 (2013) 17630-17637.

[47] D. R. Kumar, S. Kesavan, M. L. Baynosa, J.-J. Shim, Flower-like $Cu_{1.8}S$ nanostructures for high-performance flexible solid-state supercapacitors, Appl. Surf. Sci. 448 (2018) 547-558.

[48] S. Hua, D. Qu, L. An, W. Jiang, Y. Wen, X. Wang, Z. Sun, Highly efficient p-type Cu_3P/n-type g-C_3N_4 photocatalyst through Z-scheme charge transfer route, Appl. Catal. , B 240 (2019) 253-261.

[49] P. Xiao, M. Sk, L. Thia, X. Ge, R. Lim, J. Wang, K. Lim, X. Wang, Molybdenum phosphide as an efficient electrocatalyst for the hydrogen evolution reaction, Energy Environ. Sci. 7 (2014) 2624-2629.

[50] S. Ge, K. Wong, K. M. Ng, Revitalizing digenite $Cu_{1.8}S$ nanoparticles with the localized surface plasmon resonance (LSPR) effect by manganese incorporation, New J. Chem. 41 (2017) 677-684.

[51] P. Quintana-Ramirez, M. Arenas-Arrocena, J. Santos-Cruz, M. Vega-Gonzalez, O. Martinez-Alvarez, V. Castano-Meneses, L. Acosta-Torres, J. de la Fuente-Hernandez, Growth

evolution and phase transition from chalcocite to digenite in nanocrystalline copper sulfide: Morphological, optical and electrical properties, Beilstein J. Nanotechnol. 5 (2014) 1542-1552.

[52] X. Yue, S. Yi, R. Wang, Z. Zhang, S. Qiu, A novel and highly efficient earth-abundant Cu_3P with TiO_2 "P-N" heterojunction nanophotocatalyst for hydrogen evolution from water, Nanoscale 8 (2016) 17516-17523.

Figures

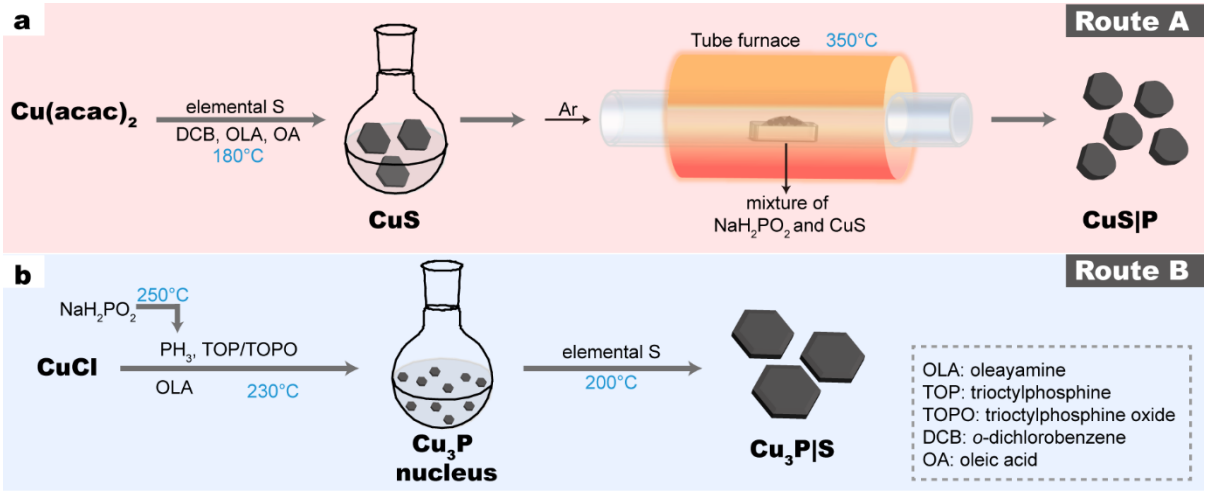

Scheme 1. Schematics illustrating the synthetic procedures of (a) CuS|P using solid-state reaction method (route A) and (b) $Cu_3P|S$ using wet chemical method (route B).

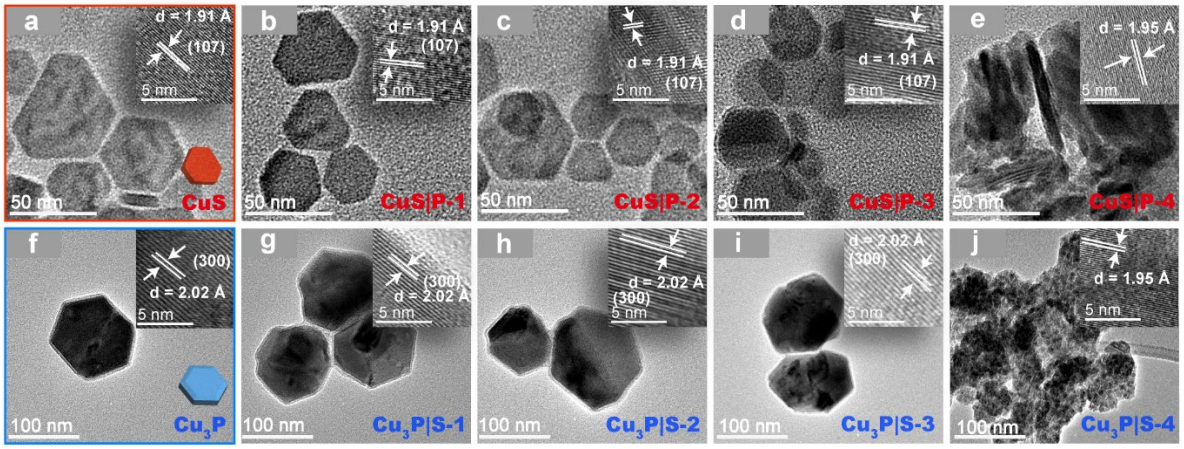

Figure 1. TEM images of (a) CuS, (b) CuS|P-1, (c) CuS|P-2, (d) CuS|P-3, (e) CuS|P-4, (f) Cu_3P, (g) $Cu_3P|S$-1, (h) $Cu_3P|S$-2, (i) $Cu_3P|S$-3, and (j) $Cu_3P|S$-4. Insets are the corresponding HR-TEM images.

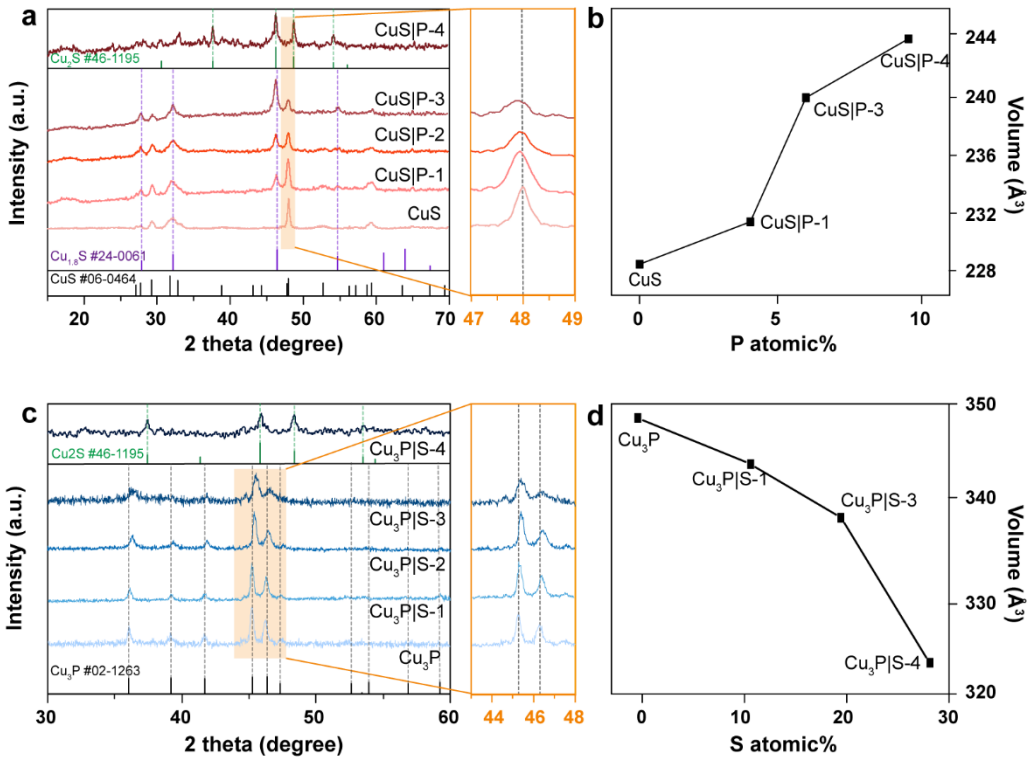

Figure 2. XRD patterns of (a) pristine CuS and CuS|P and (c) pristine Cu_3P and $Cu_3P|S$ samples. (b) and (d) are the plots of unit cell volume against P or S atomic %, respectively.

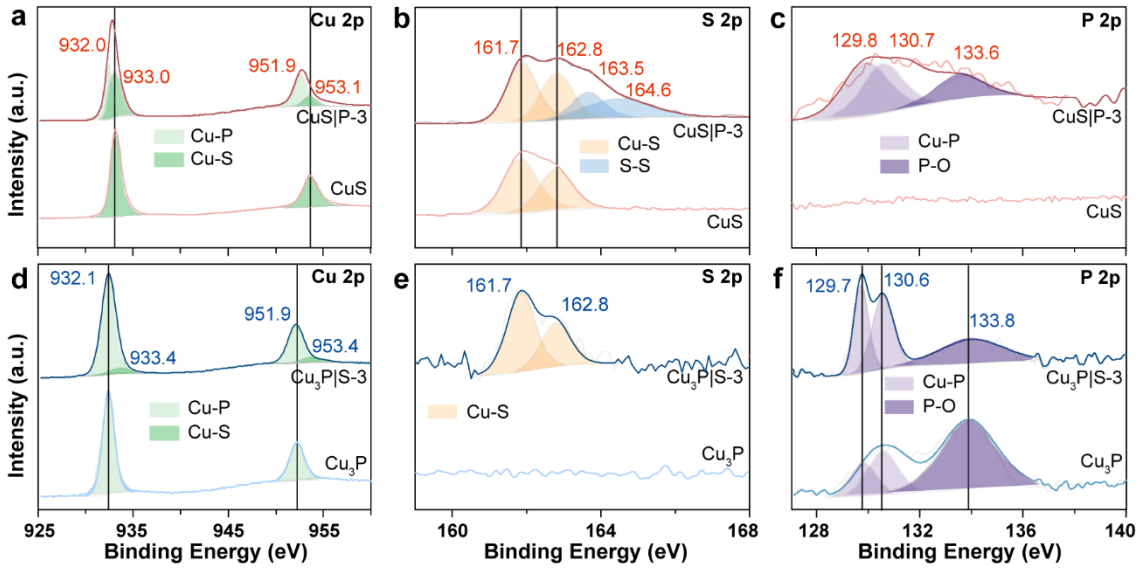

Figure 3. XPS spectra of CuS and CuS|P-3 (top) and Cu_3P and Cu_3P|S-3 (bottom) nanoplates in (a,d) Cu 2p, (b,e) S 2p, and (c,f) P 2p regions.

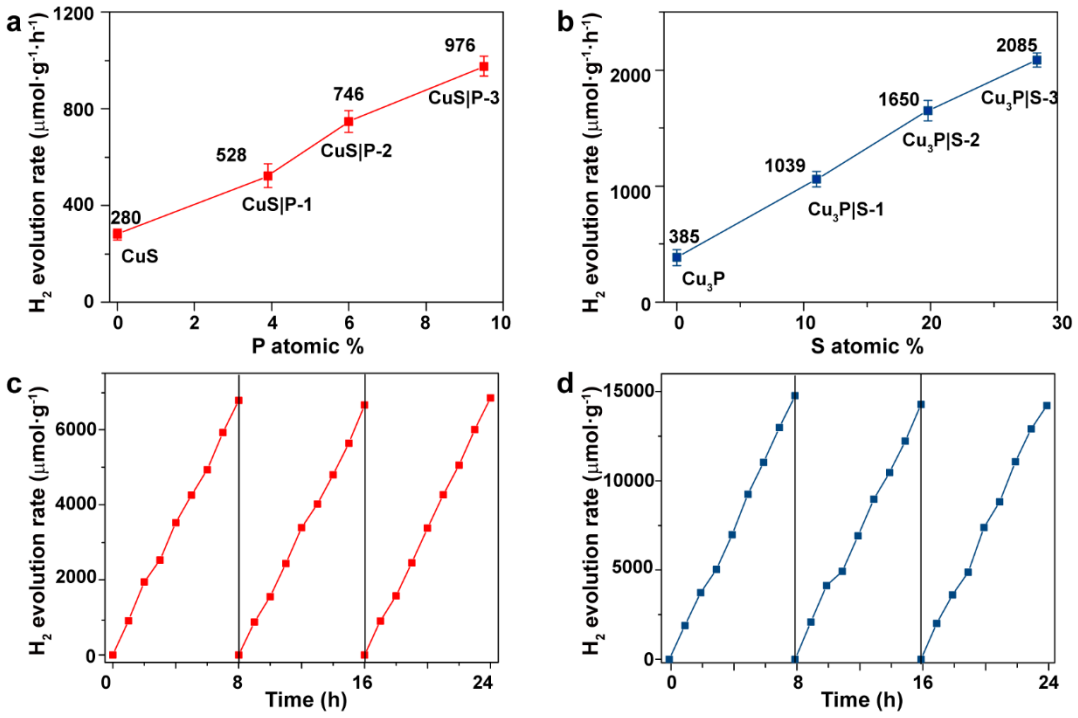

Figure 4. Photocatalytic H_2 generation rates of (a) CuS and CuS|P samples and (b) Cu_3P and Cu_3P|S samples. Long-term photocatalytic HER rates of (c) CuS|P-3 and (d) Cu_3P|S-3.

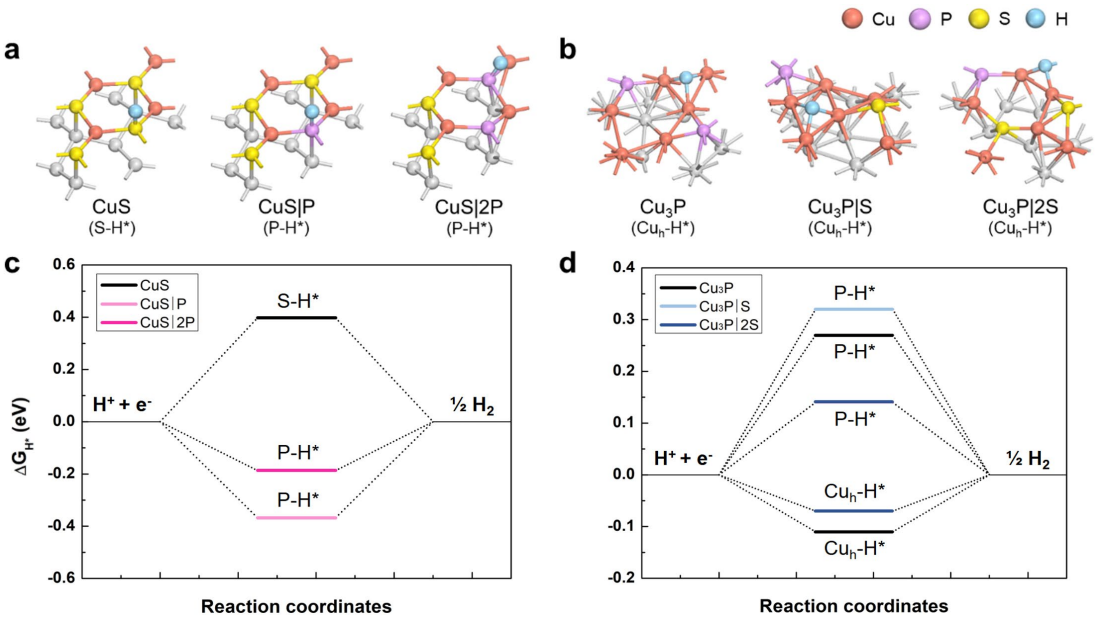

Figure 5. Most stable atomic configurations of hydrogen adsorption on (a) CuS, CuS|P, and CuS|2P, and (b) Cu_3P, Cu_3P|S, and Cu_3P|2S; Cu, P, S, and H atoms at the surface of CuS or Cu_3P are represented by orange, pink, yellow, and cyan balls, respectively. Gibbs free energy (ΔG_{H*}) diagram for hydrogen adsorption on (c) CuS, CuS|P, and CuS|2P, and (d) Cu_3P, Cu_3P|S, and Cu_3P|2S.